PNAS
www.pnas.org

Supplementary Information for

Thermal conductivity of Fe-Si alloys and thermal stratification in Earth's core

Youjun Zhang, Kai Luo, Mingqiang Hou, Peter Driscoll, Nilesh P. Salke, Jan Minár, Vitali B. Prakapenka, Eran Greenberg, Russell J. Hemley, R. E. Cohen, and Jung-Fu Lin

R. E. Cohen
Email: rcohen@carnegiescience.edu
Jung-Fu Lin
Email: afu@jsg.utexas.edu
Russell J. Hemley
Email: rhemley@uic.edu

This PDF file includes:

Supplementary Information Text

Text S1. Possible solid phase transformation of solid Fe-9Si at high P-T.

For *hcp*-Fe-9Si, we consider whether hcp Fe-9Si might transfer to a mixture of Si-poor *hcp* and FeSi *bcc* (B2) phases upon heating to 1900–2300 K at pressures of ~90-150 GPa (1, 2) (phase boundary in Fig. S4). However, we did not clearly see the bcc peaks in our measurements (Fig. S5). This may be because FeSi *bcc* did not occur due to short heating duration or the content of the FeSi phase was too low to be detected by XRD. The chemical analysis of quenched Fe-9Si sample also showed a homogeneous distribution of silicon (~9.6±1.8 wt.%) by using Energy Dispersive X-Ray Spectroscopy (EDS) (Fig. S6 and Table S3), confirming no solid evidence for the coexistence of bcc and hcp Fe-Si. We also did not observe any significant change of the resistivity in Fe-9Si at the investigated P-T conditions, except for a gentle decrease at around 2000 K (Figs. 1-2), which is overall located at the *hcp-bcc* phase boundary (1, 2). It may be possible due to the phase instability of Fe-9Si alloy at high *P-T*.

Text S2. Detailed information for the computation method.

The single-site impurity problem of DMFT is solved self-consistently where the SPTF (spin-polarized T matrix + fluctuation exchange (FLEX) (3)) solver is used. An adapted rectangular thermal grid is adopted to compute the density integration. We used the averaging Padé algorithm (4) to increase the accuracy and stability of analytical continuation. The electrical conductivity (σ) and thermal conductivity (κ) are given by

$$\sigma = \mathcal{L}_{11} \quad [S1]$$

$$\kappa = \frac{1}{eT}\left(\mathcal{L}_{22} - \frac{\mathcal{L}_{12}^2}{\mathcal{L}_{11}}\right) \quad [S2]$$

where the coefficients $\mathcal{L}_{ij}$

$$\mathcal{L}_{ij} = (-1)^{(i+j)} \int d\varepsilon \sigma_{\mu\nu}(\varepsilon)(\varepsilon - \mu)^{(i+j-2)} \left(-\frac{\partial f_T(\varepsilon)}{\partial \varepsilon}\right). \quad [S3]$$

The $f_T(\varepsilon)$ is the Fermi-Dirac distribution function at temperature T. The energy-dependent tensorial conductivity is computed from

$$\sigma_{\mu\nu}(\varepsilon) = \frac{\hbar}{\pi V} Tr\langle \hat{j}_\mu \Im G^+(E) \hat{j}_\nu \Im G^+(E)\rangle \quad [S4]$$

where $\hat{j}$ is the current density operator, V the volume of simulation cell, $\Im G^+$ the imaginary part of the advanced Green's function (5). Transport calculations of 216 atoms used a uniform K-point sampling of 4x4x4, which yields less than 0.5 μΩ cm higher than the converged resistivity. The basis includes angular momentum up to $l_{max} = 3$. A systematic overestimate of resistivity is found compared to $l_{max} = 4$, which is less than 1 μΩ cm. For the Hubbard parameters, we used $U = 4.0$ eV and $J = 0.943$ eV from previous work (6). We averaged 3 random snapshots at various conditions and found that the resistivity uncertainty maximum is ~2 μΩ cm. A small imaginary part, Im E (from $3e^{-3}$ to $2e^{-2}$ Ry) is appended to the energy argument of conductivity tensor (above equation $\sigma_{\mu\nu}$) to avoid poles inherent in the Green's function. Using various Im E values, we found a linear relation in the conductivity at Fermi energy. As a result, a linear extrapolation to Im $E \rightarrow 0$ is performed to obtain the reported results.

The final coefficient L_{ij} depends on the details of the energy-dependent conductivity tensor (see examples in Figs. S8-S9). As shown, at relatively high temperatures, the electrical conductivity (or resistivity) L_{11} (see the top panel of the left column in Fig. S8) depends mostly on the tensor within ±5 kT around the Fermi energy. In contrast, the thermal conductivity (mostly L_{22}) requires a larger range of ±10 kT. Therefore, an energy range of ±10 kT is sampled. Considering the finite-size errors, K-point sampling, we estimate the uncertainty to be within 2% and a systematic overestimate of resistivity less than 3 μΩ cm beside the inherent error introduced in approximations.

Text S3. Estimation of the stratified layer thickness.

To compute $d\rho/dr$ in the Brunt-Väisälä frequency N analysis, we write the density as

$$\rho = \rho_0(\alpha T' + \beta\chi') \quad [S5]$$

where ρ_0 is the average outer core density, T' and χ' are the convective temperature and compositional perturbations, respectively, $\alpha = 1\times10^{-5}$ K^{-1} is the thermal expansivity, and $\beta = 1.1$ is the compositional expansivity. Then

$$\frac{1}{\rho_0}\frac{d\rho}{dr} = \alpha\frac{dT'}{dr} + \beta\frac{d\chi'}{dr} \quad [S6]$$

and neutral stability at z_s implies $d\rho/dr = 0$ and

$$\alpha\frac{dT'}{dr} = -\beta\frac{d\chi'}{dr} \quad [S7]$$

which can be solved to find r_s.

First, the gradient of the temperature perturbation can be written as

$$\frac{dT'}{dr} = \frac{dT}{dr} - \frac{dT_{ad}}{dr} = -\frac{Q_T - Q_{ad}}{Ak} \quad [S8]$$

where Q_T is the total heat flow. We approximate Q_T as a constant function of radius, so that

$$Q_T = Q_{cmb} = -Ak\frac{dT}{dr} \quad [S9]$$

which is a good approximation near the CMB. Similarly, the adiabatic heat flow

$$Q_{ad} = -Ak\frac{dT_{ad}}{dr} \quad [S10]$$

is also assumed to be a constant function of depth that is set at the CMB.

Next, to compute the composition gradient we adopt a convective compositional profile of the form

$$\chi(r) = \chi_c + \chi_1\left(1 - exp\left(\frac{r-R_c}{D_\chi}\right)^2\right) \quad [S11]$$

where

$$\chi_1 = \frac{d\chi_i}{dr}\frac{\exp\left[-(D/D_\chi)^2\right]}{(2D/D_\chi^2)} \quad [S12]$$

$d\chi_i/dr$ is the compositional gradient at the ICB, $D = R_C - R_i$ is the shell thickness, and $D_\chi \approx$ 1180 km is a length scale associated with the vigor of convection. The compositional gradient at the ICB can be related to the rate of IC growth $\dot{R}_\iota$ by

$$\frac{d\chi_i}{dr} = \frac{\chi_i}{u_i}\dot{R}_\iota \quad [S13]$$

where u_i is the velocity of light elements at ICB (7).

$$u_i = \lambda\sqrt{\dot{R}_\iota \Delta\rho g_i/\eta} \quad [S14]$$

where λ =100 m is the wavelength of light element plumes, $\dot{R}_\iota$ is IC growth rate, $\Delta\rho$=600 kg/m^3 is the density difference across the ICB, g_i=4.4 m/s^2 is ICB gravity, and η =1×10^{21} Pa·s is solid viscosity. IC growth rate can be related to the core cooling rate by (8),

$$\dot{R}_\iota = -\frac{D_N^2}{2R_i(2\left(1-\frac{1}{3\gamma_C}\right)\left(\frac{D_N}{D_{Fe}}\right)^2-1)}\frac{\dot{T}_c}{T_c} \quad [S15]$$

where D_N and D_{Fe} are length scales associated with the core adiabatic temperature profile and solidus, γ_c is the core Gruneisen parameter, and T_c and $\dot{T}_c$ are the average core temperature and its rate of change, respectively. Assuming no internal heat sources, $\dot{T}_c$ can be related to Q_{cmb} by

$$\dot{T}_c = -Q_{cmb}/M_c c_p \quad [S16]$$

where M_c and c_p are core mass and specific heat. Values for all the constants are listed in Table S4.

Finally, by using eq. [S8] and eq. [S11] in eq. [S7] the stability relation becomes

$$-\alpha\frac{(Q_{cmb}-Q_{ad})}{Ak} = \beta\frac{d\chi_i}{dr}\frac{(r-R_C)}{D}exp\left[\frac{D^2}{D_\chi^2}\left(\frac{(r-R_C)^2}{D^2}-1\right)\right] \quad [S17]$$

The stratification radius $r = r_S$ is defined as where eq. [S17] is satisfied.

The modeled compositional concentration perturbation $\chi' = \chi(r) - \chi_c$ from eq. [S11] is shown in Fig. S11a, and the associated compositional buoyancy profile $-\beta d\chi/dr$ (right- hand side of eq. [S17] is shown in Fig. S 11b. The thermal buoyancy profiles $\alpha dT'/dr$ (left-hand side of eq. [S17]) over a range of Q_{cmb} is also shown in Fig. S11b at a constant value of k = 100 W/m/K (corresponding to Q_{ad} = 15.2 TW). The total thermal plus compositional buoyancy profiles $-d\rho/dr$ from eq. [S6] was then obtained (Fig. S11c). We should note that several of our assumptions in deriving these equations become less accurate at large depths and low Q_{cmb}.

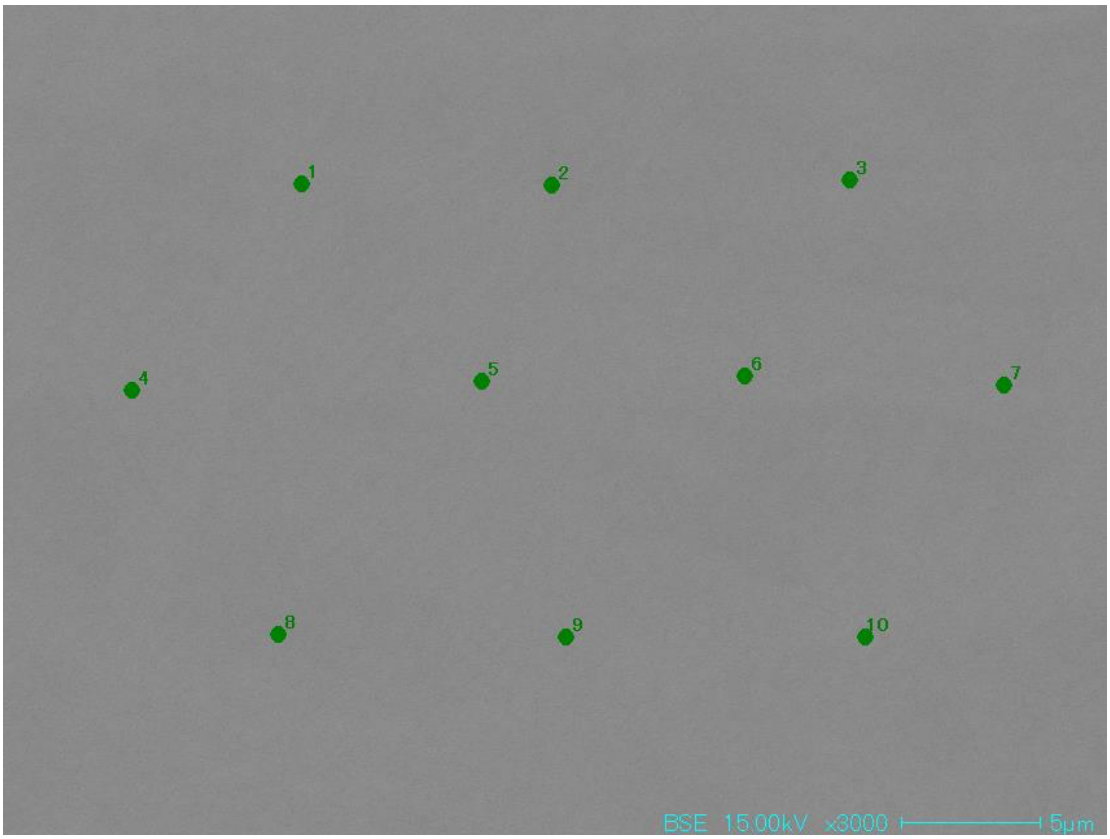

Fig. S1. Back-scattered electron image of synthesized Fe-4.3wt.%Si (Fe-8.1at.%Si) polycrystalline alloy. Random 10 points were collected in the sample to characterize its chemical composition as shown in Table S1. Results show that the sample contains 4.3(0.1) wt.% silicon and its chemical composition is homogeneous.

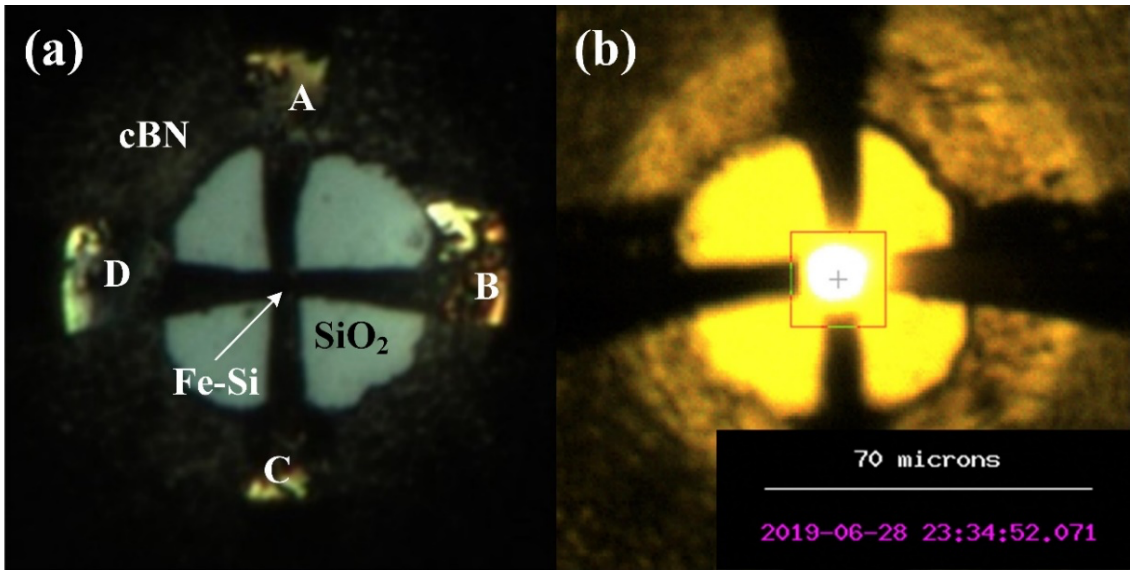

Fig. S2. Micrographs of Fe-Si alloy sample loaded in a double-sided laser-heated DAC at ~32 GPa (**a**) and at ~120 GPa and 2423(100) K (**b**) (*e.g.*, Fe-9Si here). SiO_2 was used as pressure medium and electrical insulator; the gasket was made of cBN; A, B, C, D represent the four Pt leads.

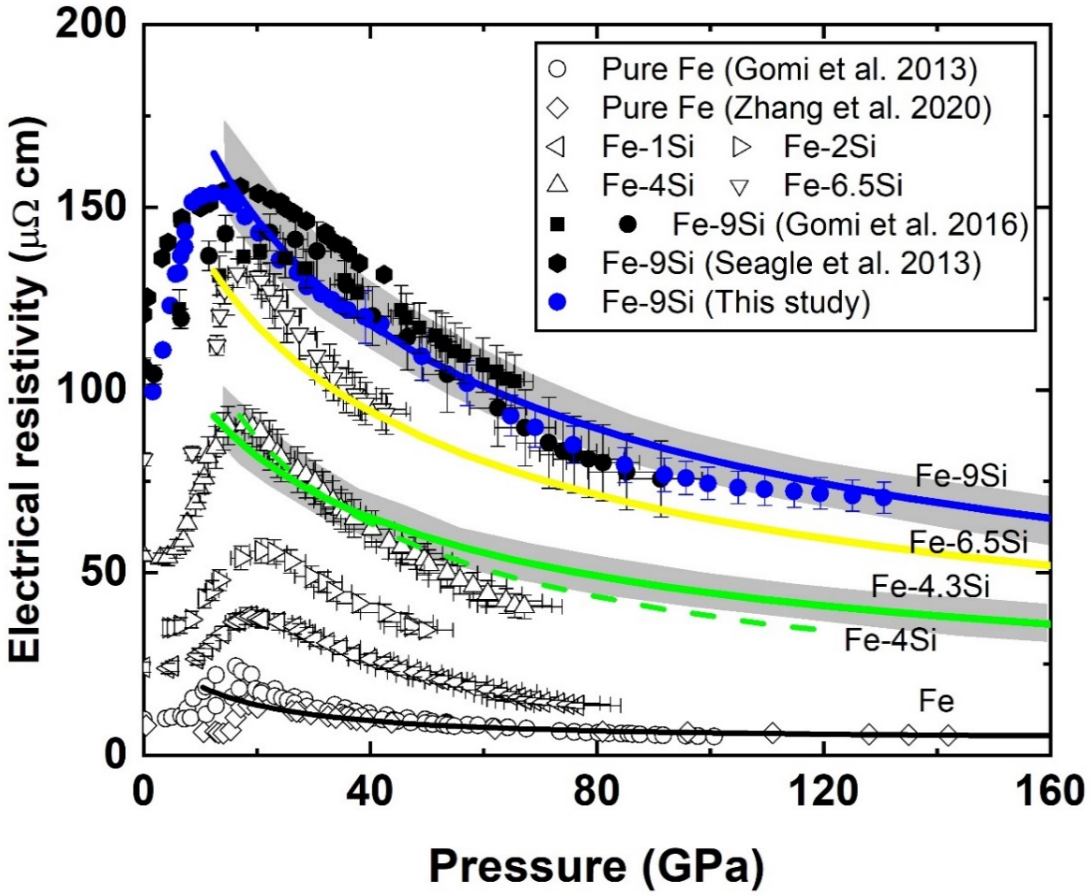

Fig. S3. Electrical resistivities of Fe and Fe-Si alloys at room temperatures as a function of pressure. The electrical resistivity of polycrystalline Fe-9Si was measured in this study upon decompression in this study (solid blue circles), which is consistent with the previous measurements by Seagle et al. (solid hexagon) (9) and Gomi et al. (Solid squares and circles) (10). High-pressure resistivity of hcp Fe-4.3Si alloy (green curve) was modeled by the sum of phonon-contributed resistivity and impurity resistivity by Matthiessen's rule based on the determined high-pressure resistivity of hcp Fe (11) and Fe-9Si alloys, which is consistent with that of hcp Fe-4Si measured at high pressures (10). The open circles and diamonds represent the measured resistivity of pure iron by Gomi et al. (12) and Zhang et al. (11) in DACs, respectively. The resistivity of Fe-1Si, Fe-2Si, Fe-4Si, and Fe-6.5Si are from Gomi et al. (2016) (10).

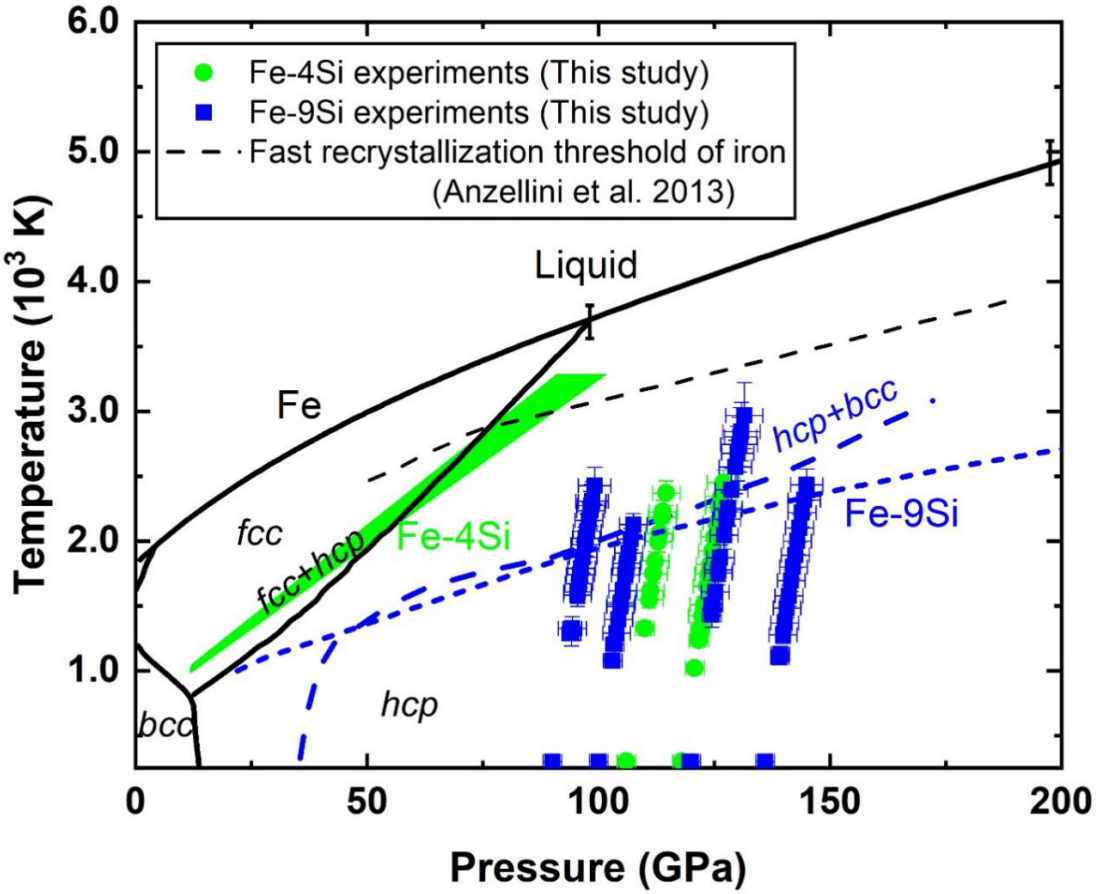

Fig. S4. **Pressure-temperature phase diagram of Fe, Fe-4Si, and Fe-9Si alloys.** Mixture phases of *hcp* and *bcc* (B2) in Fe-9Si coexist at high *P-T* (1, 2). Blue dash and short-dash lines represent the phase boundary between the *hcp* phase and the mixture phase of *hcp* and *bcc* (B2) determined by Lin et al. (1) and Fischer et al. (2), respectively. The green region represents the coexistence of *fcc* and *hcp* phases in Fe-4Si (13). Phase boundary of Fe is after Anzellini et al. (14).

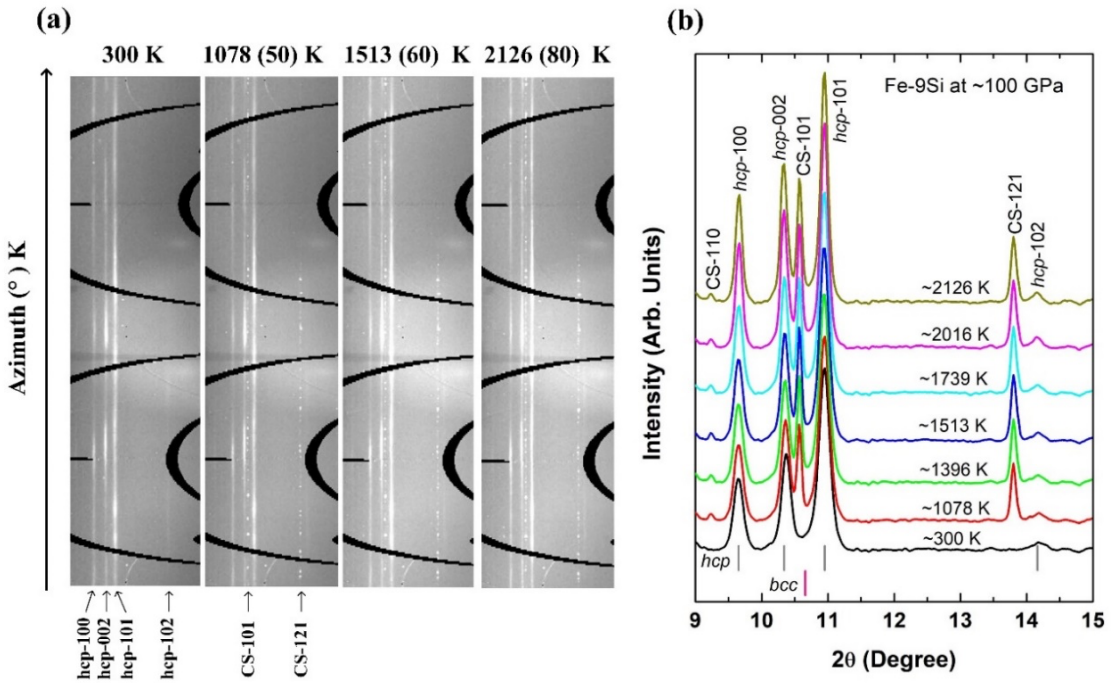

Fig. S5. Representative *in-situ* synchrotron XRD patterns of polycrystalline Fe-9Si alloy at ~100 GPa and high temperatures (λ = 0.3344 Å). The used SiO_2 insulator layer was glass at room temperature (~300 K). After heating (above ~1078 K), it crystalized as a $CaCl_2$-SiO_2 structure.

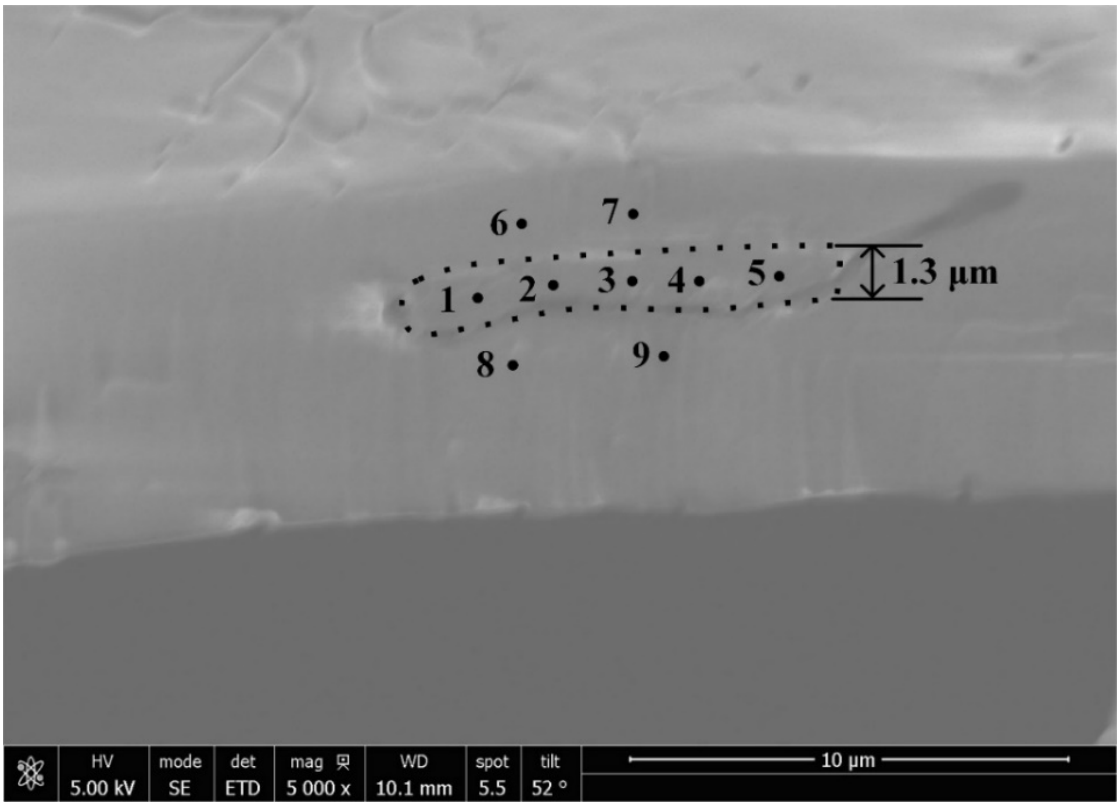

Fig. S6. Scanning electron microscope (SEM) image for the recovered Fe-9Si alloy. The quenched sample had a thickness of 1.3(0.1) µm (black dashed line). The black dots (points 1-9 and corresponding Table S2) show the locations of the SEM/EDS analyses of the sample and surrounding thermal insulator (silica).

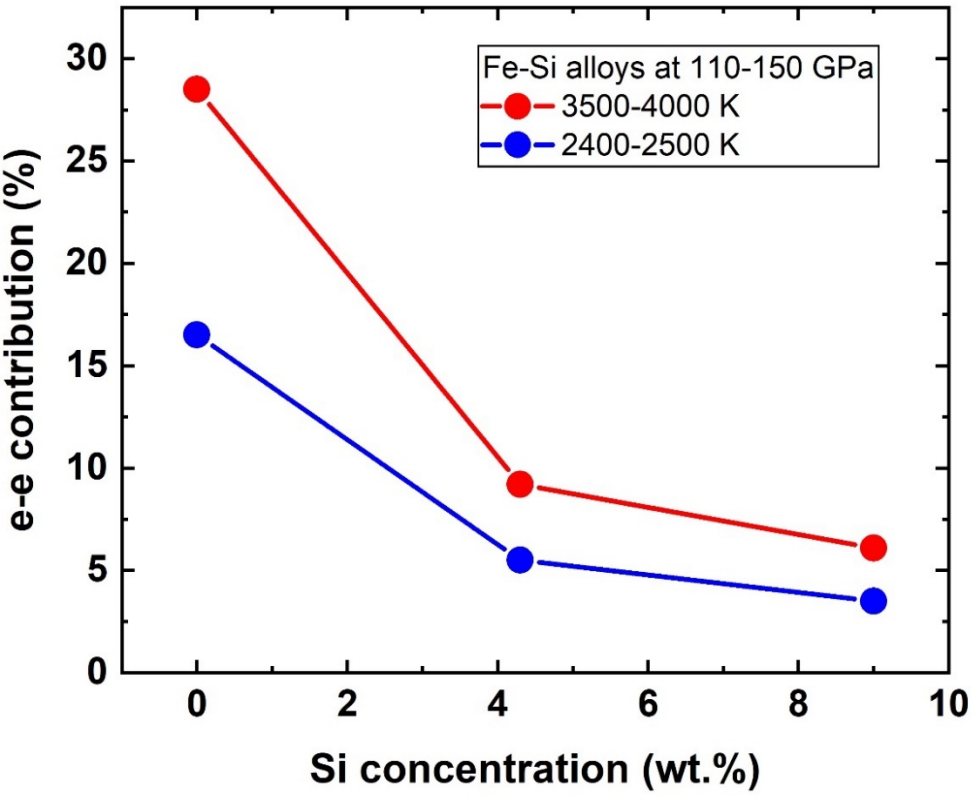

Fig. S7. The e-e contribution to the electrical resistivity of *hcp* Fe and Fe-Si alloys by DMFT and DFT calculations. The e-e contribution increases with increasing temperature at high pressure, but decreases with increasing Si concentration in *hcp* Fe-Si alloys.

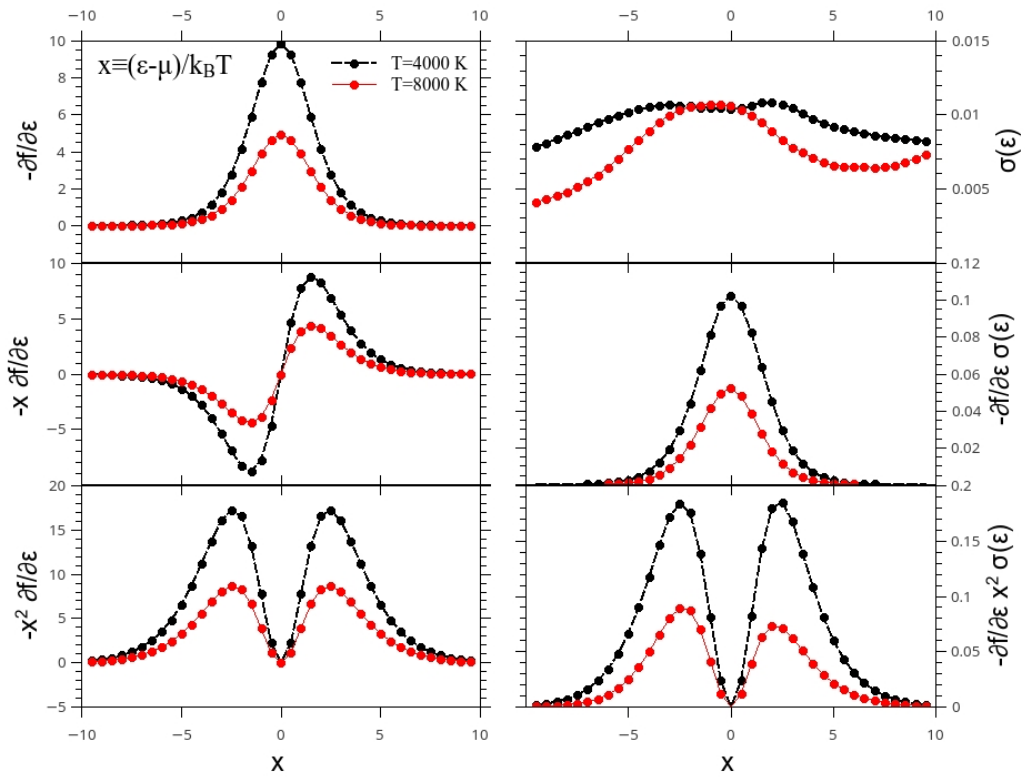

Fig. S8. Kernels for electrical and thermal conductivity of Fe-9Si. The DFT/DMFT averaged energy-dependent conductivity for Fe-9Si at 4000 and 8000 K with Im E = 0.003 Ry. The kernels (or pondering functions) have the unit of Ry^{-1}, while the electrical conductivity function σ has the unit of 10^8 S m^{-1}. At low temperatures, the dominant contribution for electrical conductivity is from energies around the chemical potential, whereas the thermal conductivity depends on the double-peaked function, ~2 k_BT away. The thermal conductivity depends on the L_{22} component only for symmetric conductivity profile, where L_{12} vanishes by symmetry.

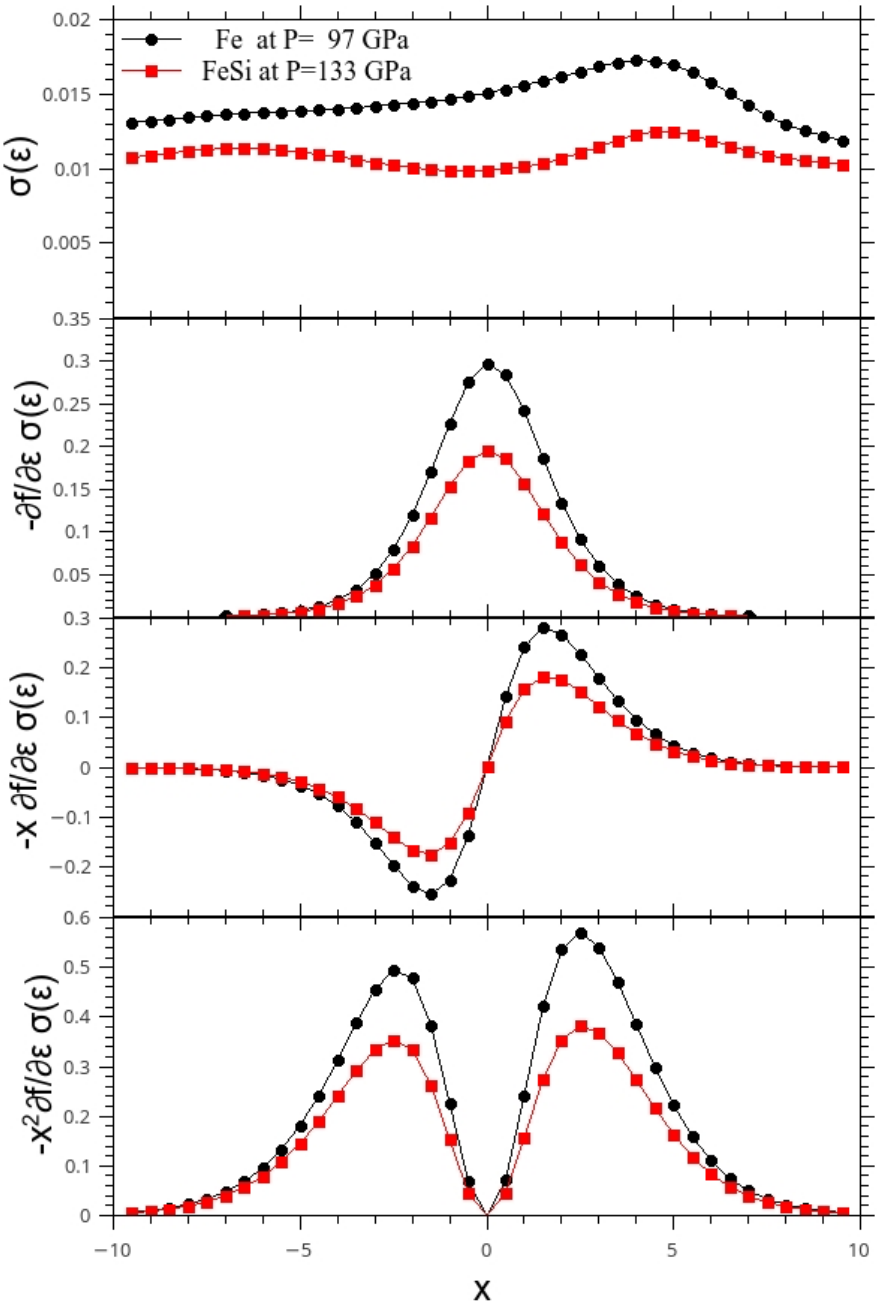

Fig. S9. Kernels for Fe and Fe-9Si alloy at T = 2000 K. Similar to the previous figure (Fig. S7), the kernels for L_{ij} are shown for a snapshot of Fe and Fe-9Si. The estimated pressures are 97 GPa for *hcp* Fe and 133 GPa for *hcp* Fe-9Si, respectively. The calculation yields a resistivity of 65.8 μΩ cm and thermal conductivity of 74 W $m^{-1}K^{-1}$ in iron; and the resistivity of 97.3 μΩ cm and the thermal conductivity of 53 W $m^{-1}K^{-1}$ in Fe-9Si.

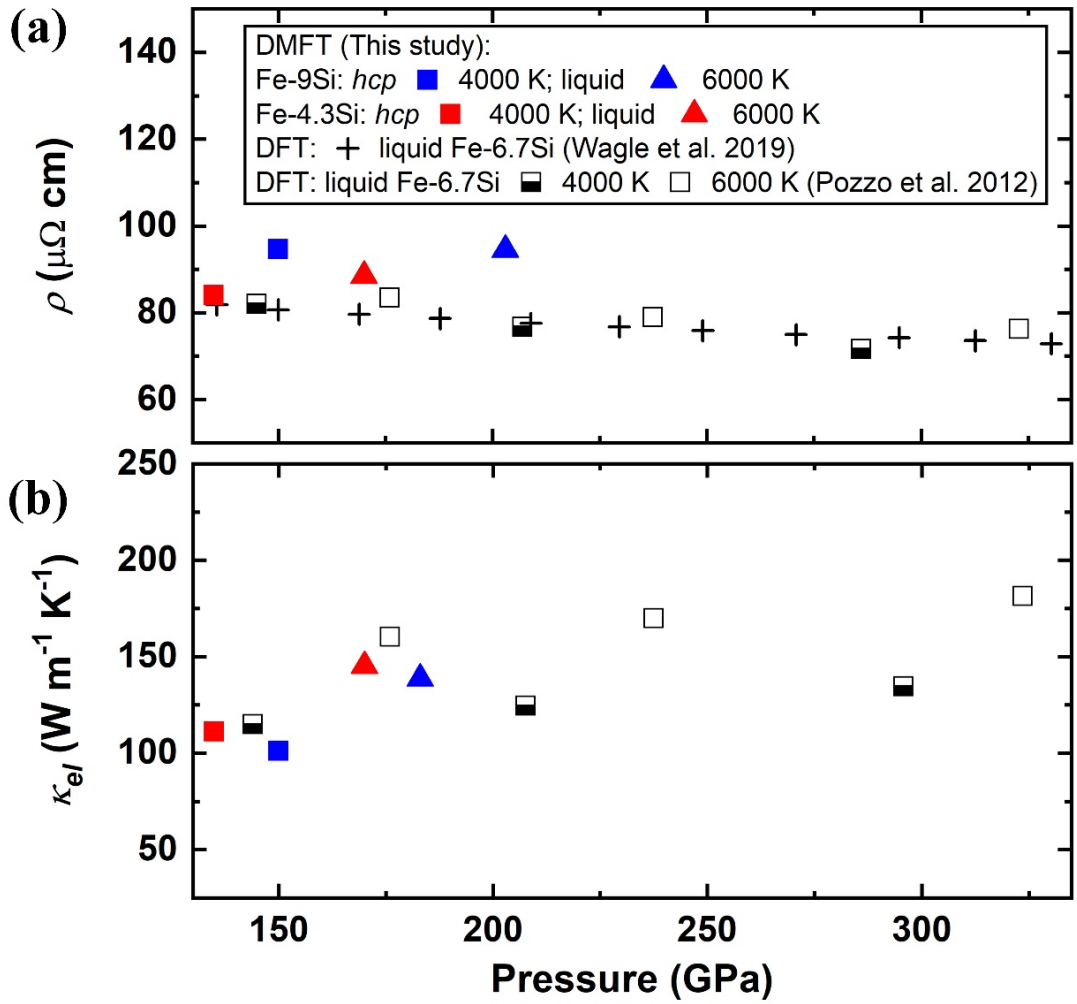

Fig. S10. Calculated transport properties of hcp and liquid Fe-Si alloys at the relevant *P-T* conditions of the core. Electrical resistivity (**a**) and electronic thermal conductivity (**b**) of Fe-Si alloys at the relevant *P-T* conditions of the outer core in the present work and compared with literature results. The solid red and blue squares represent the calculated resistivities of *hcp* Fe-4.3Si and Fe-9Si at high pressures and 4000 K by DMFT, respectively; the solid red and blue triangles represent the calculated resistivities of liquid Fe-4.3Si and Fe-9Si at high pressure and 6000 K by DMFT, respectively. Semi-open and open squares represent the calculated resistivity in liquid Fe-6.7Si at 4000 K and 6000 K using DFT by Pozzo et al. (15), respectively; the pluses "+" represent the calculated resistivity of liquid Fe-6.7Si along the outer core adiabat using DFT by Wagle et al. (16).

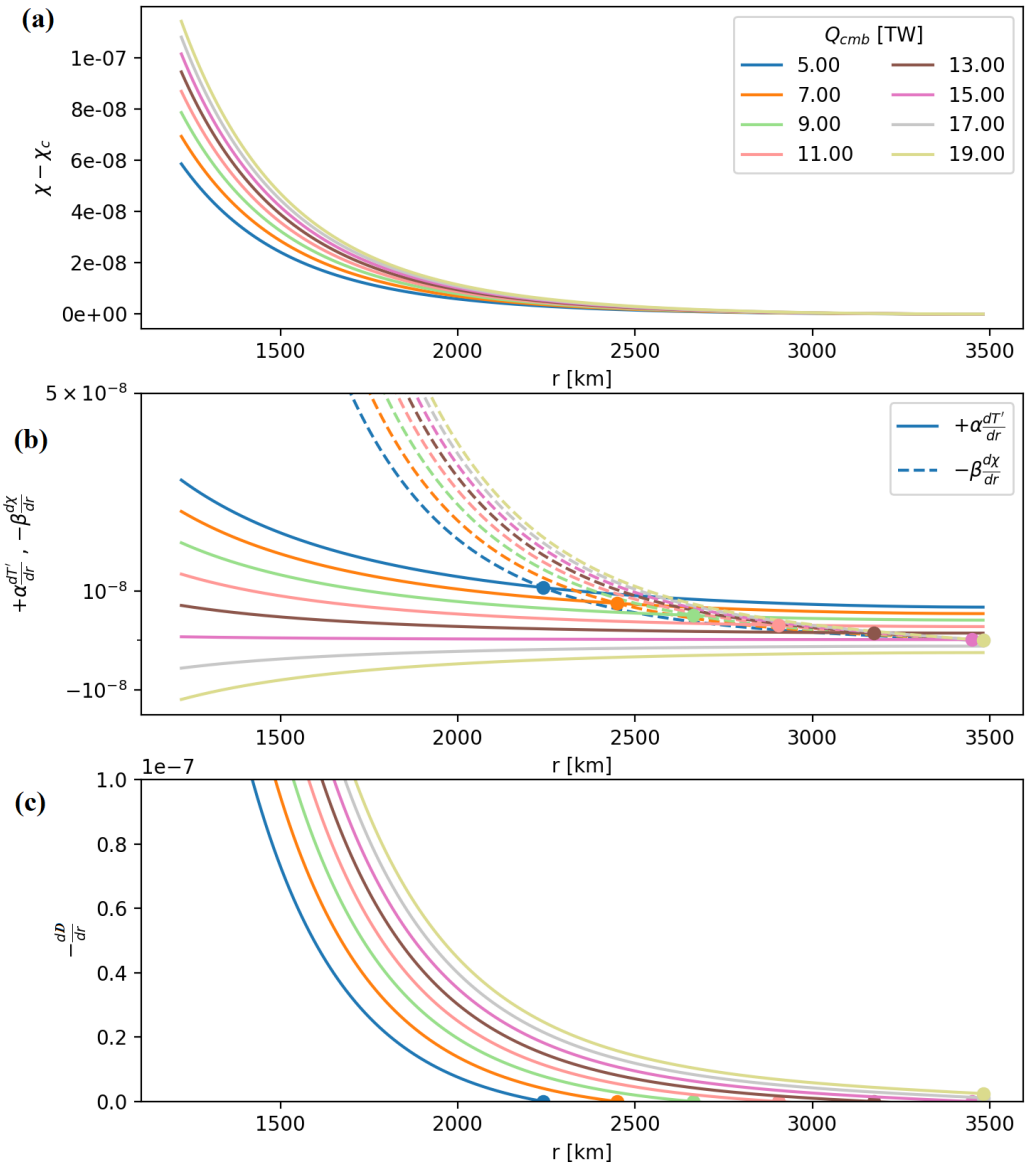

Fig. S11. Modeled buoyancy profiles in the liquid outer core. (**a**) Light element concentration perturbation $\chi' = \chi - \chi_c$ for a range of Q_{cmb}. (**b**) Thermal buoyancy profiles (solid lines) and compositional buoyancy profiles (dashed lines) from eq. [17]. Circles denote stratification radii where the curves intersect. (**c**) Total buoyancy profile $-d\rho/dr$. The colors are the same in each panel.

Table S1. The chemical composition and concentration of recovered Fe-9Si sample by Energy Dispersive X-Ray Spectroscopy (EDS).

Materials	**Points**	**Elements**		
		Fe (wt.%)	**Si (wt.%)**	**O (wt.%)**
Fe-9Si alloy	1	90.48 (2.35)	9.52 (2.35)	-
	2	89.79 (1.43)	10.21 (1.43)	-
	3	90.52 (1.79)	9.48 (1.79)	-
	4	90.23 (1.64)	9.77 (1.64)	-
	5	90.94 (1.97)	9.06 (1.97)	-
	Average	90.40 (1.8)	9.60 (1.8)	-
SiO_2 layer	6	-	53.36 (1.76)	46.64 (1.76)
	7	-	55.03 (1.53)	44.97 (1.53)
	8	-	56.24 (1.53)	43.76 (1.53)
	9	-	55.28 (1.65)	44.72 (1.65)

Table S2. Fitted parameters for the Bloch-Grüneisen formula in the electrical resistivities of hcp Fe-Si alloys at high pressure and temperature.

Composition	Pressure (GPa)	Lattice parameters of hcp-iron alloys at room temperature measured by *in situ* XRD	θ_D (K)	$\rho_{e\text{-}r}$ (μΩ cm)	$D_\rho(V)$	n
Fe-4.3Si alloy	105(3)	$a = b$ = 2.2846 Å, c = 3.6826 Å, c/a = 1.6119	655	47.3(1.0)	6.43(0.37)	0.18(0.01)
	120(4)	$a = b$ = 2.2702 Å, c = 3.6594 Å, c/a = 1.6119	675	42.8(1.1)	5.01(0.41)	0.15(0.18)
Fe-9Si alloy	100(3)	$a = b$ = 2.2966 Å, c = 3.6955 Å, c/a = 1.6091	650	83.1(1.3)	1.38(0.43)	0.03(0.02)
	120(4)	$a = b$ = 2.2740 Å, c = 3.6688 Å, c/a = 1.6134	675	73.0(1.2)	2.60(0.37)	0.07(0.02)
	136(4)	$a = b$ = 2.2588 Å, c = 3.6449 Å, c/a = 1.6136	695	71.8(1.2)	2.15(0.52)	0.04(0.02)

Note. Debye temperature (θ_D) was assumed to the same as *hcp*-Fe at high pressures (17). The Bloch-Grüneisen formula describes the temperature dependence of resistivity in *hcp*-Fe-Si alloys. We adopted the same lattice parameters in our DFT and DMFT calculations.

Table S3. Chemical composition of the starting material Fe-4.3wt.%Si (Fe-8.1at.%Si) polycrystalline alloy by electron probe microanalyzer (EPMA).

Position	Fe (wt.%)	Si (wt.%)	Total (Mass%)
1	95.887	4.244	100.131
2	96.302	4.223	100.525
3	95.797	4.274	100.071
4	95.969	4.308	100.277
5	96.204	4.298	100.501
6	96.021	4.348	100.369
7	95.864	4.229	100.093
8	96.383	4.237	100.621
9	96.18	4.137	100.317
10	96.268	4.348	100.616
Average	96.1(0.2)	4.3(0.1)	100.4(0.2)

Table S4. Model parameters for the estimation of the stratification depth.

Parameter	Value
α [K^{-1}]	$1x10^{-5}$
β	1.1
c_p [J kg^{-1} K^{-1}]	840
χ_c	$5x10^{-2}$
χ_i	$8x10^{-2}$
$\Delta\rho_i$ [kg m^{-3}]	600
D_χ [km]	1180
D_{Fe} [km]	7000
D_N [km]	6340
g_i [m s^{-2}]	4.4
γ_c	1.3
k [W $m^{-1}K^{-1}$]	100
λ [m]	100
T_c [K]	5014
dT_{ad}/dr [K m^{-1}]	$-1x10^{-3}$
u_i [m s^{-1}]	$2.64x10^{-13}$

SI References:

1. J.-F. Lin, H. P.Scott, R. A. Fischer, Phase relations of Fe-Si alloy in Earth's core. *Geophys. Res. Lett.* **36**, L06306 (2009).
2. R. A. Fischer *et al.*, Phase relations in the Fe–FeSi system at high pressures and temperatures. *Earth. Planet. Sci. Lett.* **373**, 54-64 (2013).
3. L. V. Pourovskii, M. I. Katsnelson, A. I. Lichtenstein, Correlation effects in electronic structure of actinide monochalcogenides. *Phys. Rev. B* **72**, 115106 (2005).
4. J. Schött *et al.*, Analytic continuation by averaging Pade approximants. *Phys. Rev. B* **93**, 075104 (2016).
5. S. Wimmer (2018) Spin caloric transport and related phenomena from first principles. (University of Munich, LMU).
6. J. Xu *et al.*, Thermal conductivity and electrical resistivity of solid iron at Earth's core conditions from first-principles. *Phys. Rev. Lett.* **121**, 096601 (2018).
7. R. Deguen, T. Alboussière, D. Brito, On the existence and structure of a mush at the inner core boundary of the Earth. *Phys. Earth Planet. Inter.* **164**, 36-49 (2007).
8. P. Driscoll, D. Bercovici, On the thermal and magnetic histories of Earth and Venus: Influences of melting, radioactivity, and conductivity. *Phys. Earth Planet. Inter.* **236**, 36-51 (2014).
9. C. T. Seagle, E. Cottrell, Y. Fei, D. R. Hummer, V. B. Prakapenka, Electrical and thermal transport properties of iron and iron‐silicon alloy at high pressure. *Geophys. Res. Lett.* **40**, 5377-5381 (2013).
10. H. Gomi, K. Hirose, H. Akai, Y. Fei, Electrical resistivity of substitutionally disordered hcp Fe–Si and Fe–Ni alloys: Chemically-induced resistivity saturation in the Earth's core. *Earth. Planet. Sci. Lett.* **451**, 51-61 (2016).
11. Y. Zhang *et al.*, Reconciliation of experiments and theory on transport properties of iron and the geodynamo. *Phys. Rev. Lett.* **125**, 078501 (2020).
12. H. Gomi *et al.*, The high conductivity of iron and thermal evolution of the Earth's core. *Phys. Earth Planet. Inter.* **224**, 88-103 (2013).
13. T. Komabayashi *et al.*, Phase transition boundary between fcc and hcp structures in Fe-Si alloy and its implications for terrestrial planetary cores. *Amer. Mineral.* **104**, 94-99 (2019).
14. S. Anzellini, A. Dewaele, M. Mezouar, P. Loubeyre, G. Morard, Melting of iron at Earth's inner core boundary based on fast X-ray diffraction. *Science* **340**, 464-466 (2013).

15. N. de Koker, G. Steinle-Neumann, V. Vlček, Electrical resistivity and thermal conductivity of liquid Fe alloys at high P and T, and heat flux in Earth's core. *Proc. Natl. Acad. Sci. USA* **109**, 4070-4073 (2012).
16. F. Wagle, G. Steinle-Neumann, N. de Koker, Resistivity saturation in liquid iron–light-element alloys at conditions of planetary cores from first principles computations. *C. R. Geosci.* **351**, 154-162 (2019).
17. A. Dewaele *et al.*, Quasihydrostatic equation of state of iron above 2 Mbar. *Phys. Rev. Lett.* **97**, 215504 (2006).